SSRG International Journal of Electrical and Electronics Engineering
ISSN: 2348-8379/ https://doi.org/10.14445/23488379/IJEEE-V11I8P125

Volume 11 Issue 8, 275-294, August 2024

Original Article

Integrated Renewable Energy System for Electric Vehicles Utilizing a PV-Fed Three-Phase Synchronous Reluctance Motor and High Gain DC-DC Converter

P. R. Jeevarathinam[1], K. Vinoth[2]

[1,2]*Department of Electrical and Electronics Engineering, Vel Tech Rangarajan Dr Sagunthala R&D Institute of Science and Technology, Tamil Nadu, India.*

[1]*Corresponding Author : prjeevarathinam20@gmail.com*

Received: 12 June 2024 Revised: 15 July 2024 Accepted: 11 August 2024 Published: 31 August 2024

Abstract *- This research proposes an integrated approach to enhance electric vehicle (EV) performance and efficiency using renewable energy. It combines a photovoltaic (PV) array with a High Gain Improved Single-Ended Primary Inductor Converter with Luo topology (Integrated SEPIC-Luo DC-DC converter) to optimize PV system output. An African Buffalo Algorithm (ABA) optimized Artificial Neural Network (ANN) Maximum Power point tracking (MPPT) controller is introduced, which maximizes PV system power output by continuously adapting to environmental changes. Excess energy is stored in a supercapacitor via a bi-directional converter, allowing for rapid storage and release as needed. The EV's propulsion system features a three-phase synchronous reluctance motor (SyRM) integrated with an (n+1) diode and (n+1) semiconductor converter, with speed regulation by a Hysteresis controller-based Proportional-Integral (PI) controller for precise motor control. The system also supplies excess energy to the grid through a single-phase Voltage Source Inverter (VSI), enabling grid integration and renewable energy injection. This integrated system optimizes PV system output, enhances EV efficiency, and contributes to sustainability and grid stability. The tracking efficiency of the African Buffalo Algorithm-ANN based MPPT is 98.85%, whereas the efficiency of the proposed converter is 90%. The simulation tool MATLAB was used for the whole evaluation.*

Keywords *- 1ϕVSI, ABA optimized ANN controller, Hysteresis controller-based PI controller, Integrated SEPIC-Luo Converter, Three-Phase SRMN.*

1. Introduction

The growth in population and industrialization has caused the need for electrical energy to rise significantly. Conventional energy sources, which were historically the main sources of electricity, including coal, natural gas, and crude oil, have had detrimental effects on the environment, contributing significantly to global warming [1, 2]. As a result, the usage of renewable energy sources, such as solar power, has risen.

PV systems use converters to transform the DC energy generated by solar panels into AC power, which is suitable for grid integration or residential consumption. One such converter is the buck-boost converter, which amplifies or reduces the input voltage to produce a steady output voltage, offering flexibility in voltage conversion but with increased complexity compared to simpler converters [3]. Another converter, the SEPIC, step up or down the input voltage while maintaining isolation, offering benefits such as continuous input current and non-inverted output voltage, albeit with higher complexity and component count [4]. LUO converters, on the other hand, offer a greater voltage gain capability with fewer components despite having a larger output current ripple as a drawback [5]. Different kinds of DC-DC converters, including ZVS-DAB converters, Phase-Shift converters, and FB-LLC Resonant converters, offer different advantages in terms of cost-effectiveness, efficiency, and EMI reduction. These converters are essential for efficient power conversion, allowing controllers to manage and regulate the electricity flow in a system effectively [6-8].

By enabling the concept of integration, the proposed SEPIC-LUO converter overcomes the drawbacks of existing converters that are discussed in Table 1 and achieves better power distribution, less current ripple, smaller passive components (especially the output filter), faster transient response, and lower EMI. When compared to separate SEPIC and Luo converters, the SEPIC-LUO converter in this work solves the drawbacks associated with input and output voltage needs, efficiency, component count, complexity, and transient response/stability. The use of converters in MPPT is crucial for effectively matching the load's production from renewable

energy sources, maximizing power transfer. MPPT is essential in PV systems to maximize energy generation.

While the Perturb and Observe (P&O) [14] approach is preferred for simplicity and adaptability, it leads to power losses as it oscillates around the Maximum Power Point (MPP) during sudden changes. Incremental conductance [15], although more complex and noise-sensitive, provides better MPP tracking. Fuzzy Logic MPPT [16] is appreciated for its adaptability but requires careful adjustment. Neural network-based MPPT [17], while adaptable, is intricate and requires a large amount of training data. The use of MPPT in converters ensures that renewable energy systems operate at their maximum power output, maximizing their efficiency.

Controllers, such as the PI controller, are crucial for controlling electrical power in converters. The PI controller, simpler and more efficient than PID controllers, consists of an integrator and a proportional gain, providing rapid error response and eliminating steady-state errors [18-20]. Enhanced PI controllers improve system stability and performance by adjusting control parameters. The following defines the work's primary contributions,-

- Combining PV panels with a specialized converter to improve EV performance and efficiency.
- An ABA-optimized ANN controller is used to maximize the output power of the PV system.
- Excess energy is stored using a supercapacitor, interfaced from the DC link via a bi-directional converter, providing a rapid and reliable energy storage solution.
- The speed of the SyRM is regulated by a Hysteresis controller-based PI controller, providing precise control over the motor's operation.
- The integrated system offers a dependable way to power electric vehicles. It connects them to the grid while also increasing the solar panels' power output and improving the efficiency and environmental friendliness of EVs.

Table 1. Comparison of conventional techniques

S. No.	Ref	Converter Used	Advantage	Disadvantage
1	9	LLC resonant converter	High Efficiency, Zero-Voltage Switching (ZVS)	Complexity, EMI Filtering Issue
2	10	Bidirectional DC-DC Converter	Bidirectional Power Flow, Efficient Power Conversion	Cost, Efficiency Trade-offs
3	11	Three-Phase Interleaved LLC DC-DC Converter	Reduced Switching Losses, Improved Reliability	Thermal Management, Intricacy
4	12	Resonant converters, DC-DC converters, front-end converters, and back-end converters	Efficient Charging, Flexibility	Reliability issues, Requirement of Soft Switching Techniques
5	13	DC-DC converters, Power inverters, and Bidirectional converters	Integration with RESs, Energy Storage Integration	Expense and complex

2. Proposed Methodology

This system is devised to maximize the efficiency of PV systems by the integration of advanced technologies, including the SEPIC-LUO converter, ABA-ANN MPPT controller, and supercapacitor energy storage, as shown in Figure 1. The core objective is to optimize power extraction from the PV panels, ensure efficient energy storage, and enhance overall system reliability.

Key components of the system include the bi-directional converter with a BR converter topology featuring (n+1) semiconductor and (n+1) diode configuration for efficient power flow management. Additionally, the system incorporates a PI controller for voltage regulation and a hysteresis controller for PWM pulse generation, both working in conjunction with the ABA-ANN MPPT controller to maintain optimal operating conditions for the PV system. The integration of the SRM motor further enhances the system's versatility and applicability in various renewable energy applications.

The methodology encompasses detailed system modelling, simulation, and hardware implementation to validate the system's performance under a broad range of operating conditions. Key performance metrics such as efficiency, MPPT accuracy, and bi-directional power flow capability are thoroughly evaluated to assess the system's effectiveness.

Overall, the proposed methodology aims to address critical challenges in PV systems, including MPPT efficiency, energy storage optimization, and power quality management, thereby offering a comprehensive and sustainable solution for renewable energy generation and utilization.

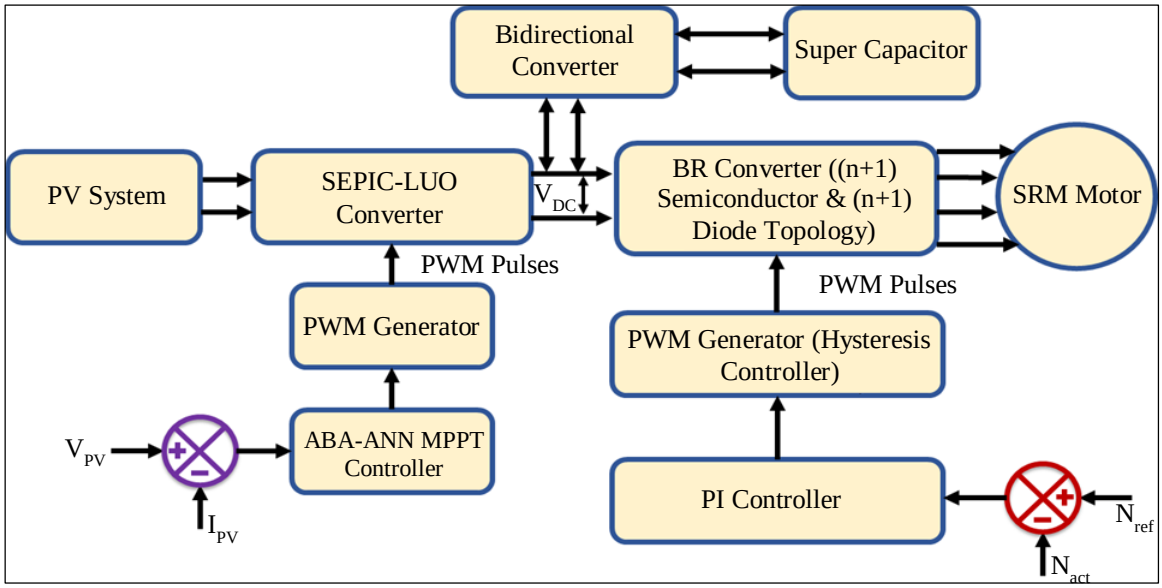

Fig. 1 Block diagram of proposed methodology

3. System Modelling

3.1. Design of PV System

The equivalent circuit of the solar cell, which comprises the resistance, current source, and diode in both parallel and series mode, is utilized in the PV equations to calculate the PV module's output current. Figure 2 illustrates the modelling of a single-diode PV system.

$$I = I_{ph} - I_D \tag{1}$$

$$I = I_{ph} - I_0 exp\left(\frac{V+IR_S}{V_t}\right) \tag{2}$$

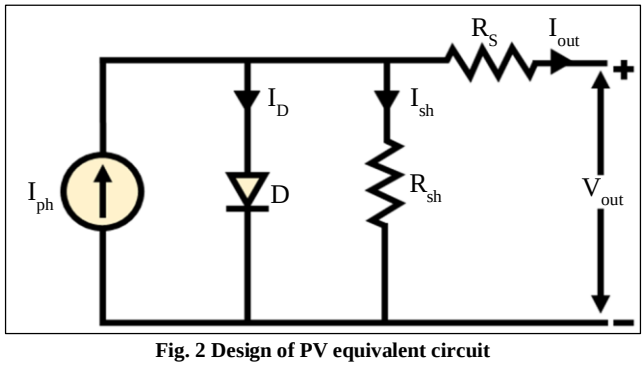

Fig. 2 Design of PV equivalent circuit

In an ideal solar cell, the saturation current (dark current) can be calculated using the open-circuit conditions in the method (3)

$$I_0 = \frac{I_{sct}}{exp\left(\frac{V_{oct}}{V_t}\right)} \tag{3}$$

Where $I_{sct}$the sole temperature-dependent is current from a short circuit and $V_{oct}$is the temperature-dependent open circuit voltage. A converter that uses Photovoltaic (PV) technology has the advantage of being able to convert solar energy into electrical energy with efficiency, allowing for the generation of renewable power.

3.2. SEPIC-LUO Converter

To enhance the PV output, a converter is employed, utilizing a combination of SEPIC and LUO converters. This combination provides the benefit of higher voltage gain and enhanced efficiency, all within a single, compact, and versatile power conversion solution. The work focuses on the utilization of the SEPIC-LUO converter, with Figure 3 illustrating the operation of the SEPIC-LUO Continuous Conduction Mode (CCM) DC-DC converter. The diagram shows the input voltage source(V_S), two inductors(L_1 $and L_2$), a coupling capacitor (C_1) linked to the inductors to provide insulation, a switching device, and a power diode and to guarantee that a current route for the DC flow is there(D_1). Typically, the switching element is a S_1-labeled Insulated Gate Bipolar Transistor (IGBT). Additionally displayed is the circuit's load resistance(R).

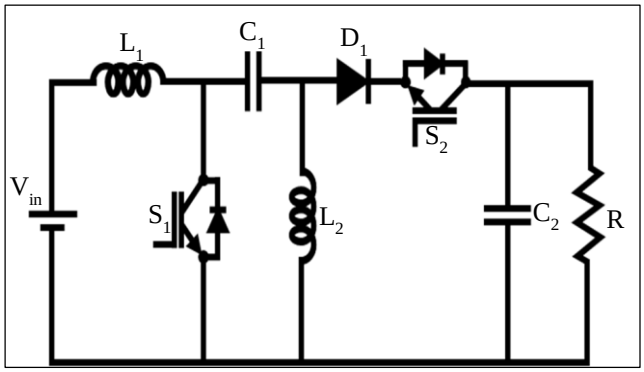

Fig. 3 Circuit diagram of SEPIC-LUO converter

3.2.1. SEPIC-LUO Converter Operating Modes

State I $(0 < t < D)$

The current I_{L1} rises when S_1 is turned ON. The second inductor,I_{L2} experiences a similar increase in current, but it does so negatively. The first inductor,L_1 stores more energy. Capacitor C_1 thus provides the energy needed to raise the current inI_{L2}. Figure 3(a) of the SEPIC-LUO converter displays the switch ON mode.

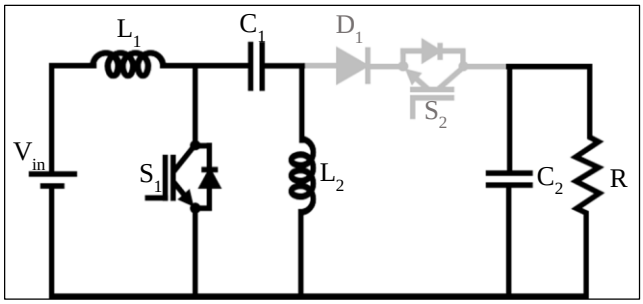

Fig. 3(a) SEPIC-LUO converter operation mode when S_1 is ON

Equations (4), (5), (6), and (7) display the relevant formulae to use KVL and KCL to state the I of CCM.

$$V_S - L_1 \frac{diL1}{dt} = 0 \tag{4}$$

$$C_1 \frac{dVC1}{dt} + i_{L1} = 0 \tag{5}$$

$$L_2 \frac{diL2}{dt} - V_{C1} = 0 \tag{6}$$

$$C_2 \frac{dVc2}{dt} + \frac{Vc2}{R} = 0 \tag{7}$$

State II $(0 < t < D)$

The current flowing through the inductor (I_{L1}) and the capacitor input current (I_{C1}) are equal when the switch S_1 is switched off. The direction of the current I_{L2} does not change; it continues to move negatively. The diode D_1 is operating. Figure 3(b) shows the Switch S_1 OFF when running in SEPIC-LUO converter mode.

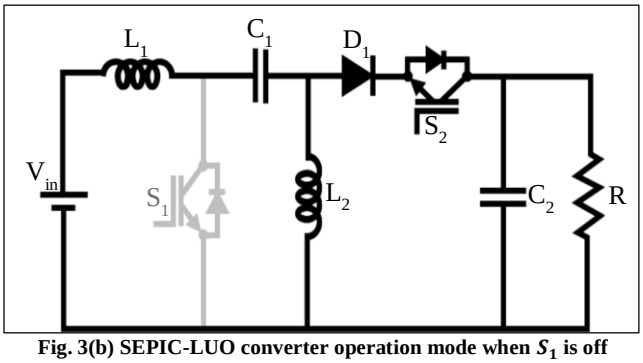

Fig. 3(b) SEPIC-LUO converter operation mode when S_1 is off

Equations (8), (9), (10), and (11) provide the appropriate formulas for CCM state II employing KVL and KCL.

$$V_S = L_1 \frac{di_{L1}}{dt} + v_{C1} + v_{C2} \tag{8}$$

$$L_2 \frac{di_{L2}}{dt} + V_{C2} = 0 \tag{9}$$

$$C_1 \frac{dv_{C1}}{dt} - i_{L1} = 0 \tag{10}$$

$$C_1 \frac{dv_{C2}}{dt} - i_{L1} - i_{L2} + \frac{Vc2}{R} = 0 \tag{11}$$

3.2.2. State Space Modelling

Equations (12) and (13) provide the overall state space equations for the SEPIC-LUO working in state I of CCM.

$$\dot{x}(t)A1x(t) + B1u(t) \tag{12}$$

$$y(t) = C_1 x(t) \tag{13}$$

Equations (14) and (15) provide the state matrix for the SEPIC-LUO operating in state I.

$$\begin{bmatrix} \frac{di_{L1}}{dt} \\ \frac{di_{L2}}{dt} \\ \frac{dv_{C1}}{dt} \\ \frac{dv_{C2}}{dt} \end{bmatrix} = \begin{bmatrix} 0 & 0 & 0 & 0 \\ 0 & 0 & \frac{1}{L2} & 0 \\ 0 & \frac{-1}{C1} & 0 & 0 \\ 0 & 0 & 0 & \frac{1}{RC2} \end{bmatrix} \begin{bmatrix} i_{L1} \\ i_{L2} \\ v_{C1} \\ v_{C2} \end{bmatrix} + \begin{bmatrix} \frac{1}{L_1} \\ 0 \\ 0 \\ 0 \end{bmatrix} V_S \tag{14}$$

$$y(t) = [0\ 0\ 0\ 1] \begin{bmatrix} i_{L1} \\ i_{L2} \\ v_{C1} \\ v_{C2} \end{bmatrix} \tag{15}$$

Additionally, (16) and (17) provide the overall state formulas for the SEPIC-LUO converter operating in CCM state II.

$$\dot{x}(t)A2x(t) + B2u(t) \tag{16}$$

$$y(t) = C_2 x(t) \tag{17}$$

Next, as seen in (18) and (19), the state matrix of the in-state II SEPIC-LUO converter can be established.

$$\begin{bmatrix} \frac{di_{L1}}{dt} \\ \frac{di_{L2}}{dt} \\ \frac{dv_{C1}}{dt} \\ \frac{dv_{C2}}{dt} \end{bmatrix} = \begin{bmatrix} 0 & 0 & \frac{-1}{L1} & \frac{-1}{L1} \\ 0 & 0 & \frac{-1}{L1} & \frac{-1}{L1} \\ \frac{1}{C2} & 0 & 0 & 0 \\ \frac{1}{C2} & \frac{1}{C2} & 0 & \frac{-1}{RC2} \end{bmatrix} \begin{bmatrix} i_{L1} \\ i_{L2} \\ v_{C1} \\ v_{C2} \end{bmatrix} + \begin{bmatrix} \frac{1}{L_1} \\ 0 \\ 0 \\ 0 \end{bmatrix} V_S \tag{18}$$

$$y(t) = [0\ 0\ 0\ 1] \begin{bmatrix} i_{L1} \\ i_{L2} \\ v_{C1} \\ v_{C2} \end{bmatrix} \tag{19}$$

For the SEPIC-LUO converter, the state matrix's average form throughout a switching cycle is provided in (20) and (21).

$$\begin{bmatrix} \frac{di_{L1}}{dt} \\ \frac{di_{L2}}{dt} \\ \frac{dv_{C1}}{dt} \\ \frac{dv_{C2}}{dt} \end{bmatrix} = \begin{bmatrix} 0 & 0 & \frac{D-1}{L1} & \frac{D-1}{L1} \\ 0 & 0 & \frac{D}{L2} & \frac{D-1}{L1} \\ \frac{1-D}{C1} & \frac{-D}{C1} & 0 & 0 \\ \frac{1-D}{C2} & \frac{1-D}{C2} & 0 & \frac{-1}{RC2} \end{bmatrix} \begin{bmatrix} i_{L1} \\ i_{L2} \\ v_{C1} \\ v_{C2} \end{bmatrix} + \begin{bmatrix} \frac{1}{L_1} \\ 0 \\ 0 \\ 0 \end{bmatrix} V_S \quad (20)$$

$$y(t) = [0\ 0\ 0\ 1] \begin{bmatrix} i_{L1} \\ i_{L2} \\ v_{C1} \\ v_{C2} \end{bmatrix} \quad (21)$$

In this case, A stands for the SEPIC converter's duty cycle within the range of (0–1), B for the input matrix, C for the output matrix, and D for the system matrix. One benefit of utilizing a SEPIC-LUO converter's output in an optimized Artificial Neural Network (ANN) for Maximum Power Point Tracking (MPPT) is that it can enhance the MPPT algorithm's stability and efficiency in solar power systems.

3.3. An African Buffalo Optimized Algorithm

MPPT based on ANN and the ABO algorithm combines the ANN's capacity to learn and adapt to intricate patterns in renewable energy systems with the exploration and exploitation capabilities of ABO to optimize the MPPT process. Through the use of ANN's predictive capability and ABO's capacity to find optimal solutions in a dynamic and uncertain environment, this synergy seeks to improve MPPT efficiency and accuracy in renewable energy systems, ultimately enhancing system performance.

The ABO was modeled after the migratory behavior of African buffalos, namely their ability to organize themselves when traveling from one area of Africa to another in search of grazing pastures. Previous books and National Geographic television documentaries both closely explored the organization and movement of African buffalos, which served as the foundation for the creation of the ABO. The goal of the ABO's design was to create a quick, reliable, effective, efficient, and user-friendly algorithm that could sufficiently explore and exploit the solution space by simulating the democratic and communicative abilities of African buffaloes, sometimes referred to as Cape buffaloes, in their quest for solutions.

ABO mimics the African buffalos' collaborative instincts, eloquence in communication, and group decision-making processes, which heavily emphasize the utilization of the herd's combined intelligence. The two vocalizations that the buffalos mostly utilize to group themselves when looking for answers are the repulsion (/waaa/ sound) for exploration and the attraction (/maaa/ sound) for exploitation. The effective use of both calls is essential for the mobility of the herd, the provision of resources, and the community's overall safety in Buffalo.

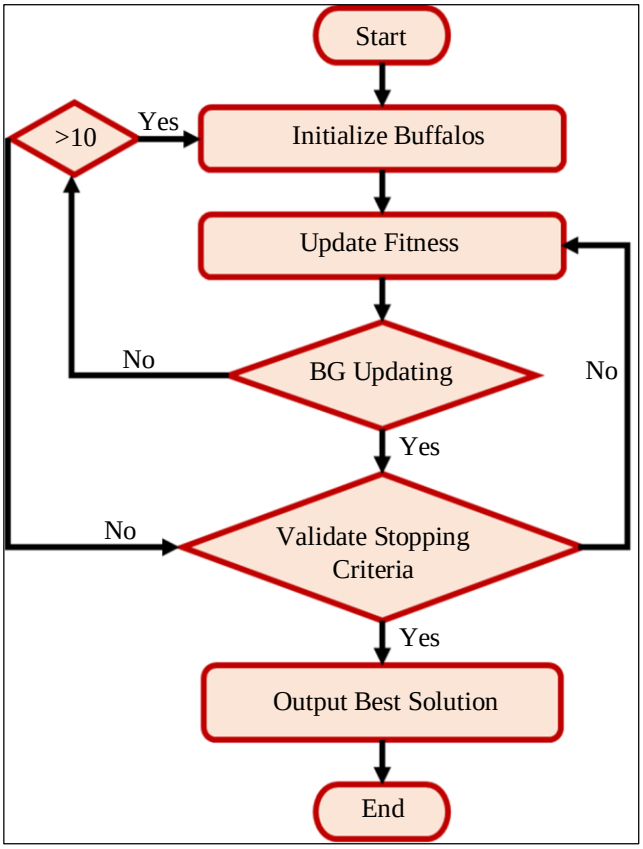

Fig. 4 Displays the ABO algorithm and flowchart

1. Initialize the buffalo's within the search space;
2. Calculate the buffalos exploitation:
$$m'_k = m_k + lp1(bg - W_k) + lp2(bp_k - W_k)$$
3. Calculate the buffalo's locations using:
$$W'_k = \frac{(W_k + m_k)}{\lambda}$$
4. Determine if the bg is updating YES, proceed to 5. Else return to 2
5. Crosscheck stopping criteria. Not reached, return to step 2, else proceed to 6
6. Output best solution.

Note that /waaa/call is represented by W_k in Figure 4. This call encourages the herd to proceed (investigate), paying special attention to Buffalok. Them$_k$ stands for the exploitable /maaa/ call. Likewise,W'_k the request for additional exploration; lp1 andlp2, the learning parameters are m'_k,λ a, which indicates that further exploitation is required; and} a random number, which can have any value between 0 and 1, depending on the problem being solved. Greater values are associated with less exploration and more exploitation, and vice versa.

3.3.1. ABO Mathematical Description

The population of buffalo in the search space is first randomly initialized by the ABO. Next, the buffalo's potential for exploitation is evaluated using Equation (22). The results of this assessment are essential in figuring out what the buffalos will do next in their quest for productive grazing areas. To ascertain whether the buffalos would stay put or migrate, the outcome of democratic Equation (22) is given in the exploratory Equation (23) [see Equation (23) below]. If the best-positioned buffalo, orbg, When updating (with respect to the global optimum), the algorithm determines whether the stopping requirement has been satisfied. So, the run is ended, and the output is the location of the finest buffalo. If this is the case, the best buffalo has been found, and the run has come to an end. If the halting condition is not reached, the algorithm returns to step 2 and assesses the buffalos' exploitation values. The driving force for the whole buffalo herd's relocation to other, perhaps more lucrative, sites than where they are now is this equation:

$$m'_k = m_k + lp1(bg - W_k) + lp2(bp_k - W_k) \qquad (22)$$

Three components make up Equation 22, the exploration equation: the memory part(m'_k), which informs the buffalos that they have moved from their prior location(m_k), the second section($lp1(bg - W_k)$), which indicates the buffalo's cooperative behavior, and the third section ($lp2(bp_k - W_k)$) stands for bufalos' exceptional ability to communicate with the rest of the herd. Take note that the learning parameter lp1 influences this choice.

The final component of Equation (22),$lp2(bp_k - W_k)$ highlights the extraordinary intellect exhibited by these creatures. They are able to distinguish between their current place and their most productive past location. When the buffalos stray into a famished area, they use this knowledge to find their path back to the most lucrative previous spot. Furthermore, please take note of the fact that the learning parameter lp2 influences the buffalo's extraordinary intelligence concerning the prior finest rewarding place in comparison to their current position. As seen, the entirety of Equation (22) emphasizes the buffalo's abilities to use their collective intelligence, outstanding memory, and consistent communication with one another to make well-informed decisions while searching for solutions.

Once more, it is evident that the method multiplies the maximum vector by the parameters for learning$(lp1, lp2)$, which are typically between 0 and 1. It does this by subtracting the dimensional elementW_k from it. Through the process of parameter tuning, the correct the learning parameters' values$(lp1, lp2)$ be obtained. Additionally, keep in mind that a larger lp1 number tends to favour a global search, whilst a higher lp2 value favours a local search. The sum to find the real fitness of the buffalos, one of these products, is then added to the exploitation memory portion of the equation (m_k) for the specified dimension($xory$). In essence, Equation 23 moves the bufalos to a new place based on the result of Equation (22).

$$W'_k = \frac{(W_k + m_k)}{\lambda} \qquad (23)$$

The buffalo movement is determined by their /waaa/ calls (W_k) and /maaa/ calls(m_k), which are controlled by the exploration driver ~, which has a value between 0 and 1. This is observed in Equation (23). There is less exploration, the greater the value of the, and vice versa. The ABO is represented as follows: Therefore, in Figure 3, buffalo k's movement from W_k (the current exploration location) to other locations must be influenced by other factors likem_k, the exploitation location, and an appropriate adjustment of its position with respect to both the personal best$(bg - W_k)$ and the herd's best $(bg - W_k)$ using the hidden bias of the learning parameters.

Tracking the maximum power point in solar photovoltaic systems is made more efficient by utilizing the African Buffalo Optimized Algorithm in ANN-based MPPT. The potential for improved efficiency and accuracy in tracking the PV's MPP results in improved system performance and energy utilization when an African Buffalo optimized algorithm is used in an ANN-based MPPT technique within an integrated renewable energy system for electric vehicles.

3.4. ANN Based MPPT Technique

Renewable energy systems will more effectively identify and track the ideal operating point for optimum power output by combining the ANN-based MPPT algorithm with the ABO algorithm. The ANN's learning skills are complemented by the exploration and exploitation powers of the ABO algorithm, which improves performance, and increases adaptability to changing environmental conditions.

Combining these two improves the system's dependability and efficiency, which maximizes the amount of energy extracted from renewable sources. Artificial Neural Networks (ANNs) have demonstrated efficacy across multiple disciplines by offering accurate and faster solutions for complex mathematical problems. ANN are used in the MPPT system because they react rapidly and precisely to a variety of external factors. There are numerous activation functions at your disposal. The following equations express the output of a neuron:

$$v_k = \sum_{x=1}^{x=n} (w_{ki} \cdot x_i + b) \qquad (24)$$

$$y_k = f(-v_k) \qquad (25)$$

Where y_k is the output and $x_i$is the ith input for neuron k; w_{ki} is a weight from neuron k's input; f is the activation function, and b is the bias.

Figure 5 shows a summary of the ANN used for MPPT with V_{pv} and I_{pv} acting as the standard inputs. By using a converter to alter the PV voltage, utilize the duty cycle (D) output signal.

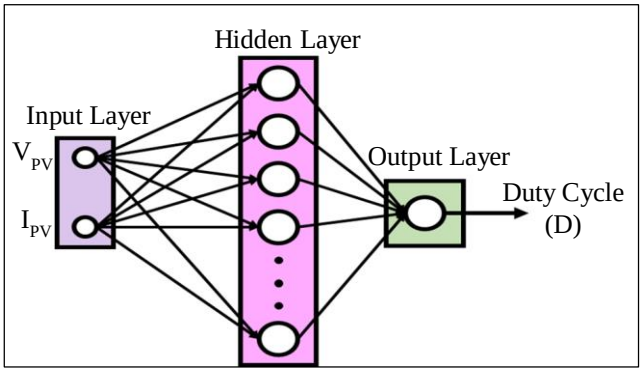

Fig. 5 The ANN architecture for MPPT

An ANN is used as a control system to tell D to change V_{pv}A boost converter is used to track maximum output power. The following chart illustrates the relationship between the inverter's DC voltage (V_{dc}), duty cycle (D), and PV array voltage (V_{pv}):

$$V_{pv} = (1 - D * V_{dc}) \tag{26}$$

The PV model described in Section II contains the training data (i.e., targets and inputs) required to train the ANN for MPPT. The trained ANN is activated for MPPT whenever a satisfactory performance is achieved, as shown by the Mean Square Error (MSE). An explanation of the ANN's MPPT training process technique can be found in Figure 6.

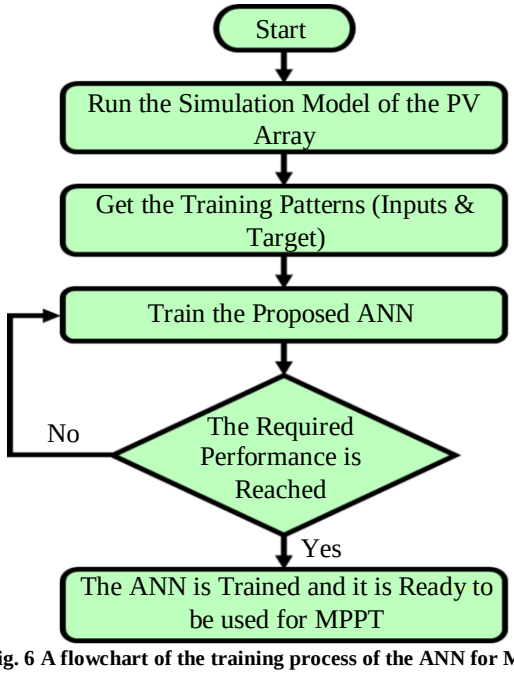

Fig. 6 A flowchart of the training process of the ANN for MPPT

Increased energy efficiency and a decreased dependency on conventional fuel sources are two benefits of utilizing a renewable energy system for electric vehicles that makes use of a PV-fed three-phase synchronous reluctance motor and high gain DC-DC converter. Utilizing the ABO-ANN combination, system reliability and energy extraction are maximized with a Bidirectional Converter that optimizes power flow in both directions, increasing the efficiency of renewable energy systems.

3.5. Bi-Directional Converter

There are two ways to use the Bi-directional Converter: charging (also known as buck operation) and discharging (also known as boost operation). Figure 7 depicts the bidirectional battery converter circuit.

Charging Mode: A battery with a load on the output side and DC-Link are sent to the BDC while charging. BDC with buck operation is used to adjust the battery's output side voltage level on parts like the inductor L_{buck} and capacitor C_{buck}.

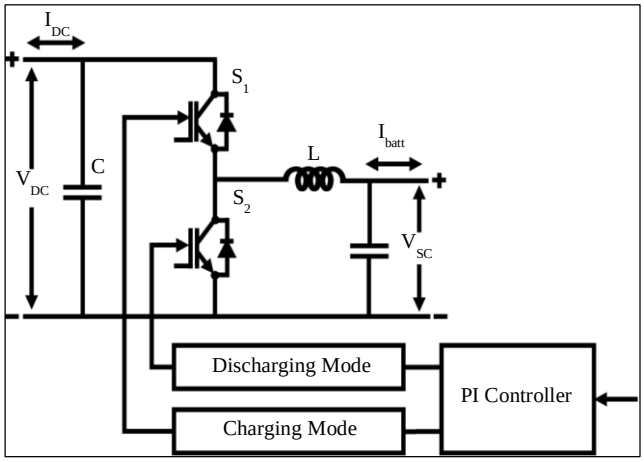

Fig. 7 Bidirectional battery converter with PI controller

The inductor and capacitor expression is expressed as follows:

$$L_{buck} = \frac{(V_{DC} - V_{SC}) D_{buck}}{\Delta I_L f} \tag{27}$$

$$C_{buck} = \frac{(1 - D_{buck}) V_{SC}}{8 L_{buck} \Delta V_{batt} f^2} \tag{28}$$

In this case, the ripple current and switching frequency for buck mode operation are represented by f and ΔI_L.

Discharging Mode: BDC interacts with the battery and DC-link comparably when in discharging mode. Here, the DC-Link is the output, while the battery is the input. The voltage at the battery terminal is lesser than the DC-link voltage level. Consequently, the boost operation is carried out using compatible components.

In buck mode, the values of the inductorL_{buck} and capacitorC_{buck} are computed as,

$$L_{boost} = \frac{V_{SC}D_{boost}}{\Delta I_L f} \quad (29)$$

$$C_{boost} = \frac{V_{DC}D_{boost}}{R_0 \Delta V_{DC} f} \quad (30)$$

Where the output impedance in boost mode is represented byR_0 and the ripple voltage byΔV_{DC}. However, the bi-directional converter operates in both modes. Consequently, it is assumed that the values of the inductor $L_{BDC}$and capacitor$C_{BDC}$are,

$$L_{BDC} = \max(L_{buck}, L_{boost}) \quad (31)$$

$$C_{BDC} = \max(C_{buck}, C_{boost}) \quad (32)$$

Moreover, the BDC functioning depends on duty ratios that are obtained by charging and discharging control, such as$D_{buck}\ and\ D_{boost}$. The ability to effectively manage energy flow makes a bidirectional converter in a supercapacitor within an integrated renewable energy system for electric vehicles advantageous. By controlling the bidirectional energy flow effectively and storing extra energy for use when needed, a bidirectional converter combined with a supercapacitor improves energy efficiency and system stability.

3.6. Super Capacitor

Supercapacitors are capacitors with larger capacitance values than any other form of capacitor currently on the market. They are also referred to as ultra-capacitors or electric double-layer capacitors. Up to 400 Farads of capacitance can be found in a single conventional case size. Supercapacitors possess the highest capacitive density available today, with densities so high that they are applied in situations where batteries are frequently used. Supercapacitors are more expensive and have less volumetric efficiency than batteries. However, they have other benefits that make them the better choice for applications where a large amount of energy storage needs to be kept and released in bursts on a regular basis.

- Density of power
- The ability to recycle
- Safe
- environmentally friendly
- Compact size

The main advantage supercapacitors offer over batteries is that they charge and drain endlessly without losing performance. This is the rationale for the combination of batteries and supercapacitors. They have the advantage of effectively storing and releasing energy, which improves the motor's performance and responsiveness while lowering overall energy consumption. This is especially useful when utilizing them to switch reluctance motors as part of an all-encompassing renewable energy system for electric cars. A synchronous reluctance motor operates more efficiently when paired with a supercapacitor, which offers high-power density energy storage for peak power demands. This also increases system efficiency and dynamic response.

3.7. Modelling of Switched Reluctance Motor

Magnetic reluctance is the basis of operation for SRMs, a particular kind of electric motor. SRMs lack a winding field and a permanent magnet on their rotors, in contrast to conventional electric motors. Rather, windings are found in the stator, while laminated iron cores make up the rotor. Figure 8 shows an example of a typical cross-section of an 8-phase/6 SRM in four phases. The motor works by establishing a magnetic flux channel between the stator and rotor poles that has the least amount of magnetic resistance. In the absence of interphase coupling, the voltage between the SRM's phase terminals is represented as,

$$v = Ri + \frac{d\phi}{dt} \quad (33)$$

The relationship between stator winding resistance and flux linkage ϕ R allows for the incorporation of magnetic saturation effects by taking into account the impacts of both current and rotor positionθ. The definition of flux linkage, in this case, is

$$\phi(\theta, i) = L(\theta, i)i(t) \quad (34)$$

Evaluating the derivative of flux linkage obtains by substituting equation (34) into equation (33).

$$v = Ri + L(\theta, i)\frac{di}{dt} + \frac{dL(\theta,i)}{dt} \quad (35)$$

Increasing the inductance's time derivative results in,

$$\frac{dL(\theta,i)}{dt} = \frac{\partial L(\theta,i)}{\partial \theta}\frac{d\theta}{dt} + \frac{\partial L(\theta,i)}{\partial i}\frac{di}{dt} \quad (36)$$

On rearranging,

$$v = Ri + l(\theta, i)\frac{di}{dt} + e_b \quad (37)$$

$$l(\theta, i) = L(\theta, i) + i\frac{\partial L(\theta,i)}{\partial i} \quad (38)$$

$$e_b = i\omega_r \frac{\partial L(\theta,i)}{\partial \theta} \quad (39)$$

Equation (38) takes current, self-inductance $L(\theta, i)$, and inductance variation due to current taking into consideration while representing incremental inductance and accounting for magnetic saturation effects. Conversely, the phrase "back-EMF" of the machine indicates $e_b$in Equation (39). Robust

controllers are necessary for effective control because of the obstacles that these dependencies on position and phase current in $l(\theta, i)$ and e_b provide for current regulation.

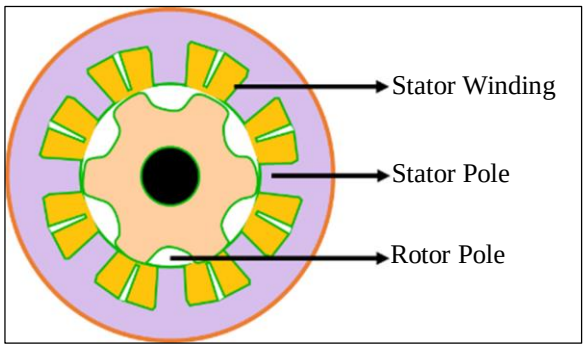

Fig. 8 Cross section of four phase SRM

Torque is produced in SRMs when the rotor and stator poles naturally line up to maximize circuit inductance. Torque in unsaturated SRMs is given by (40). However, it is difficult to express torque according to inductance and phase current parameters due to high nonlinearity in saturated SRMs.

$$T_e = \frac{1}{2} i^2 \frac{dL\theta}{d\theta} \tag{40}$$

The following is the computation of the tangential force F_t and radical force F_r using the Maxwell stress tensor:

$$F_r = \frac{1}{2\mu_0} \int_s (B_r^2 - B_t^2) ds \tag{41}$$

$$F_r = \frac{1}{\mu_0} \int_s B_r B_t \, ds \tag{42}$$

The symbols B_r, B_t, μ_0 and dsin equation (41), respectively, stand for vacuum permeability, radial and tangential flux density, and infinitesimal surface area increment. These elements produce the tangential force, which in turn produces torque. Because SRMs are sequentially excited, pulsations are intrinsic to the torque and current waveforms.

Two types of torque ripple are seen in SRMs: high-frequency torque (from switching actions) and commutation torque (from pulsed torque waveforms). High-frequency torque results from particular hardware and settings, whereas commutation torque is common and connected to intrinsic pulsations.

Electromagnetic vibration and noise are mostly caused by radial forces, which are far larger than tangential forces. For broader SRM applications, addressing these torque variations and vibrations is essential. By providing exact control over the motor's speed and torque, a Boost Rectifier (BR) converter used in conjunction with a Synchronous Reluctance (SR) motor ensures optimal performance under a variety of operating situations, hence increasing system efficiency.

3.8. BR Converter N+1 Diode & N+1 Switch Configuration

In the IDTC technique for SRMs, the usage of $(n+1)$ diode and $(n+1)$ switch configuration entails the employment of $'n'$ diodes and switches in addition to one additional diode and one additional switch. The performance of SRM is precisely controlled and optimized using this setup, especially in torque control and power conversion. A comparable circuit with all of the switching devices and diodes is shown in Figure 9.

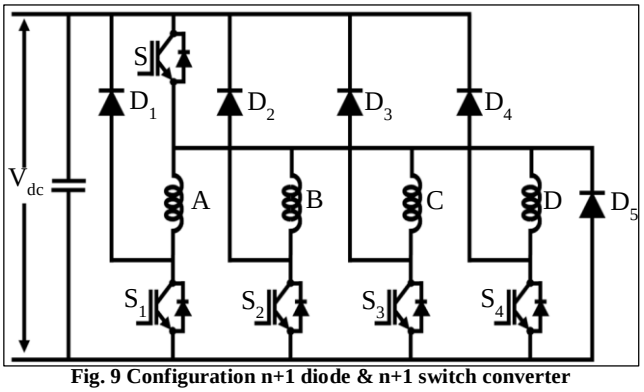

Fig. 9 Configuration n+1 diode & n+1 switch converter

When certain switches (S and S_1 for Phase A, S *and* S_2 for Phase B, S and $S_3$for Phase C and S and S_4 for Phase D) are closed to start a motor, each phase winding receives power from the DC supply. Phase A stores energy, which is then sent to the power supply via diodes D_5 and D_1 when switches S and S_1 are opened.

In a similar manner, when switches S *and* S_2 are opened in Phase B, the energy that was stored during its activation is released back into the system via diodes D_5 and D_2. Similar to Phase D, Phase C operates by returning electricity to the mains when switches S and S_4 and S and S_3 are activated.

With the use of $(n+1)$ power switches and $(n+1)$ diodes, this system manages several phases, represented by the number "n". This allows for effective control of the current flow. Through intelligent management of the release and consumption of stored energy in each phase, the unique arrangement guarantees both energy conservation and seamless operation.

In the (n+1) diode and (n+1) switch configuration technique for SRM, the control strategy makes use of a common switch S for every phase. This arrangement makes the control system simpler, and it uses Pulse-Width Modulation (PWM) to operate the switching parts, which allays the worry expressed in the comment. The duty cycle of every switch is managed by PWM signals, which establish how long a switch stays open or closed throughout a switching period. Accurate torque control and motor performance optimization are made possible by precisely controlling the effective voltage provided to each phase winding through the

adjustment of each PWM signal's duty cycle. The order in which the switches are activated and deactivated dictates the way the current flows through each phase winding.

The desired phase current profile is obtained by properly sequencing the switches, guaranteeing effective power conversion and smooth motor running. MGA-CANN ensures that the desired current profile is maintained and provides closed-loop control of the motor by modifying the PWM signals applied to the switches based on the measured current.

4. Results and Discussion

In this work, the integrated renewable energy system for Electric Vehicles (EVs) utilizing a PV-fed three-phase synchronous reluctance motor and high gain DC-DC converter showed promising performance. The system was able to efficiently harness solar energy through the Photovoltaic (PV) panels and convert it into electrical energy to power the EV's motor. The proposed systems' full simulations are verified using MATLAB, and the system's functionality is investigated.

Table 2. Parameter specification

Parameter	Rating	Parameter	Rating
Solar PV System		**SR Motor**	
Open Circuit Voltage	$37.25V$	Configuration	$8/6\ Pole\ SR\ Motor$
Short Circuit Voltage	$8.95A$	Rated Speed	$4000rpm$
Peak Power	$150W$	Rated Power	$2.5HP$
Total Power	$10KW$	Rated Voltage	$415V$
Series connected solar PV cells	36	Rated Current	$20A$
SEPIC-LUO Converter		Stator Resistance	0.01Ω
L_1	1mH	Inertia	$0.0082Kg.m.m$
L_2	35mH	Friction	$0.01Nms$
C_1	$22\mu F$	Unaligned Inductance	$0.673e^{-3}H$
C_2	$3000\mu F$	Aligned Inductance	23.6
		$Saturated\ Aligned\ Inductance$	$0.15e^{-3}$
		$Maximum\ flux\ linkage$	$0.486V.S$

Case 1

Figure 10 shows that the solar panel is receiving a constant $1000\ W/Sq.m$ of irradiation and has reached a stable temperature of$35°C$. According to these particular circumstances, it appears that the solar panel has attained a stable state. The solar panel's consistent voltage, which remains at 80V, is shown by the waveform in Figure 11. Furthermore, at 40A, the auxiliary current stabilizes. This indicates that the solar panel has stabilized at this particular voltage and current level. A steady voltage waveform of 450V at 0.5 seconds is shown in Figure 12, signifying that the voltage stays constant at this level. Similarly, the current waveform at 0.5 seconds consistently displays a value of 6.5A, proposing that the current stays constant at this level. This implies that at these particular values and timeframes, the voltage and current have both reached a steady state.

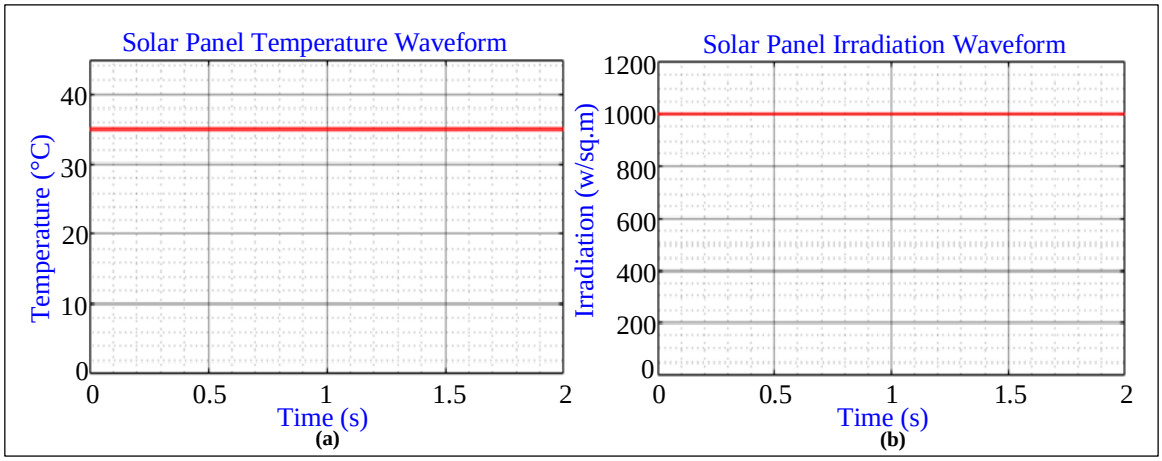

Fig. 10 Solar panel temperature and irradiation waveform

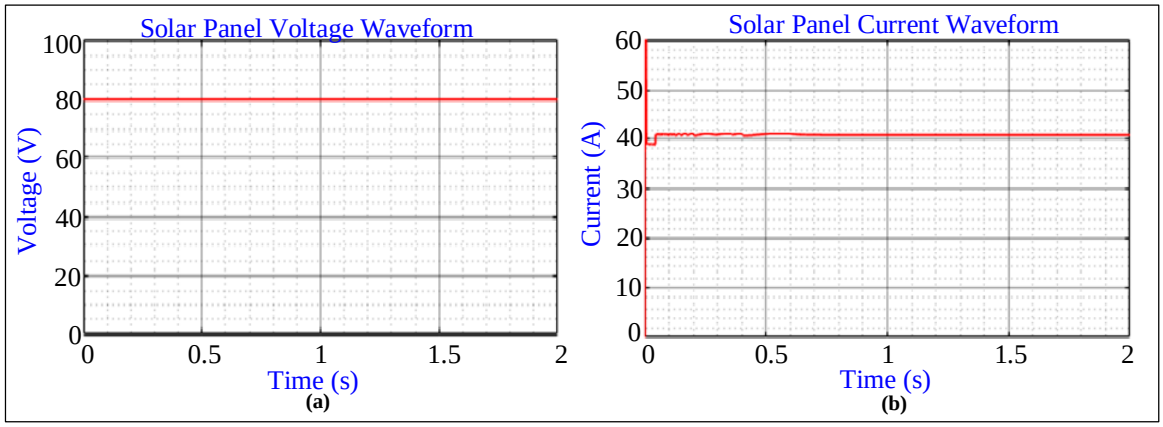

Fig. 11 Solar panel voltage and current waveform

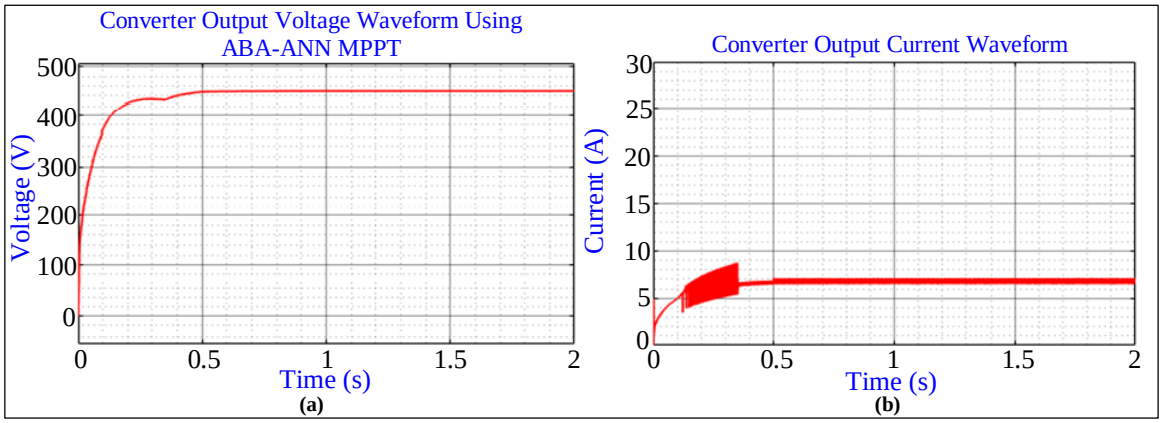

Fig. 12 (a) Converter output voltage waveform using ABA-ANN MPPT, and (b) Converter output current waveform.

Case 2

This temperature stabilization at $35°C$ takes place in 1 second, as seen in Figure 13, indicating that this temperature stays stable. Additionally, the irradiation level stays constant at $1000\ W/Sq.m$. Concurrently, it appears from this that at these particular values and times, the temperature and radiation have both attained a stable condition. Figure 14's waveform illustrates how the current stays constant at 40A while the voltage stabilizes at 80V after one second. This proposes that the voltage and current have simultaneously maintained these particular values and have reached a stable condition.

The stabilization of the voltage at 450V at 1 second is shown in Figure 15, showing that the voltage stays constant at this level. Concurrently, the output current reaches 6.5A, indicating that the voltage and current have stabilized and are staying at these particular levels.

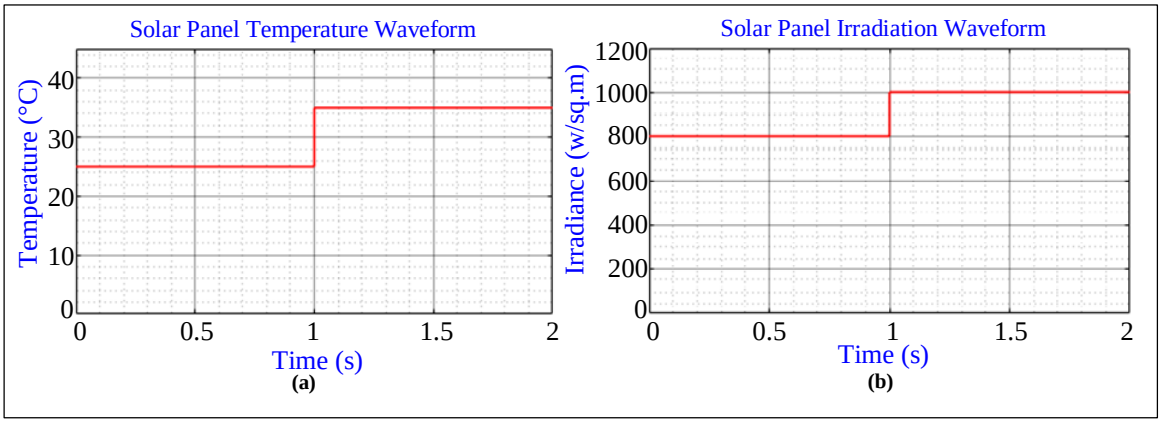

Fig. 13 Temperature and irradiation of solar panel waveform

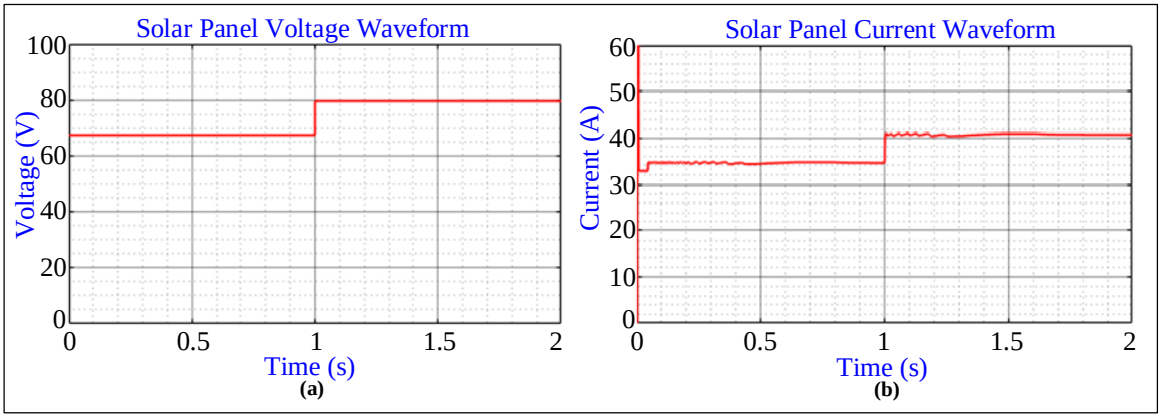

Fig. 14 Waveform of voltage and current in solar panel

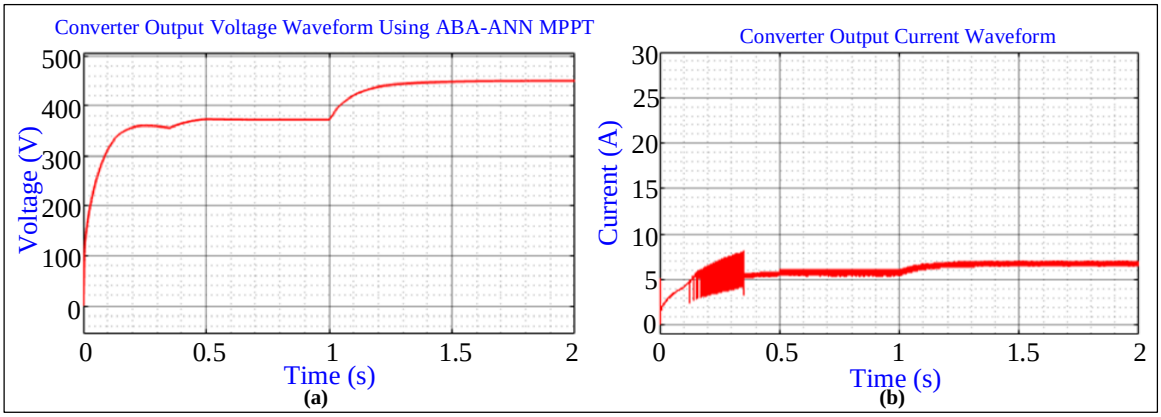

Fig. 15 (a) Output voltage waveform of converter using ABA-ANN MPPT, and (b) Output current waveform of converter.

Case 3 Under Shaded Conditions

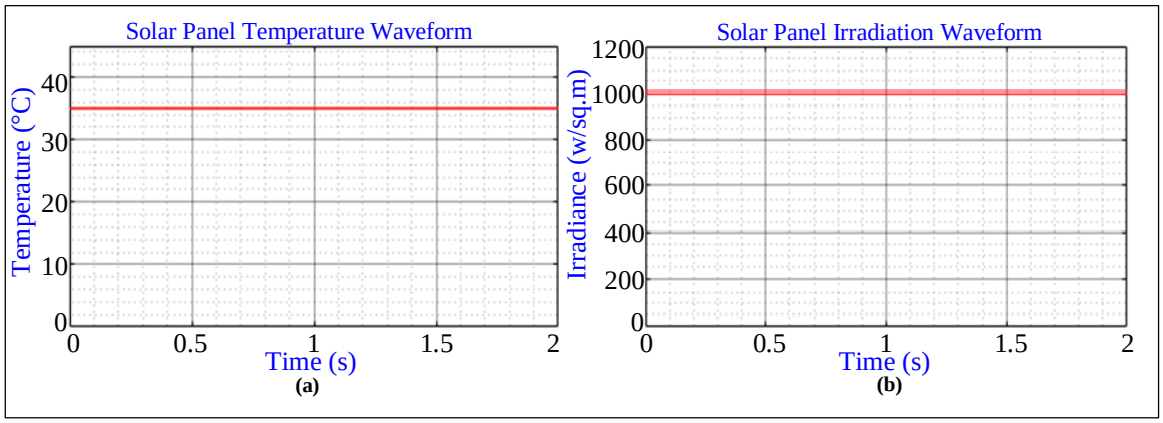

Fig. 16 Waveform of solar panel temperature and Irradiation

A steady temperature flow at 35°C is shown by the waveform in Figure 16, which proposes a level of temperature that is consistently and sustainably maintained. Furthermore, the radiation waveform has a continuous form at 1000 W/Sq.m, indicating a consistent and constant intensity of radiation throughout the observation period.

In some applications, such as controlled environments for experiments or specific industrial operations, where steady environmental conditions are necessary, these characteristics are essential. The waveform of cells under partial shade, which affects solar panel performance, is shown in Figure 17. Thirty cells are stabilized at 1 S in spite of the shading. This stabilization shows that the system keeps the desired operation of 30 cells even in situations when there is partial shading. This observation demonstrates how well the system controls shading effects and maintains the solar panel cells' performance.

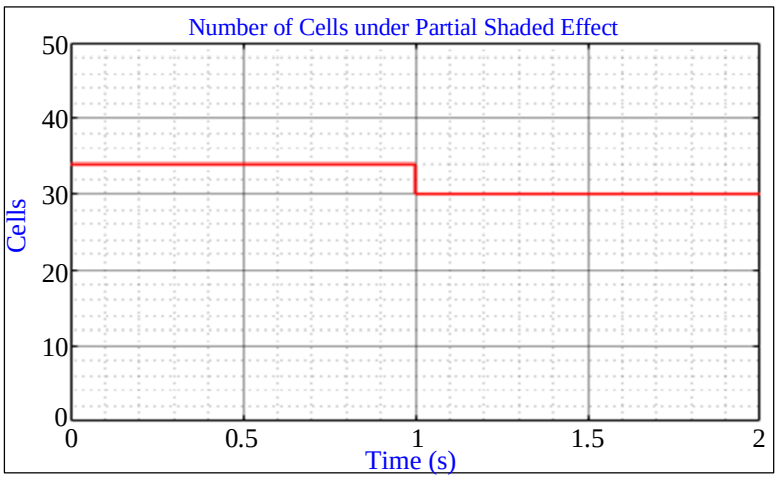

Fig. 17 Number of shells under partial shaded effect

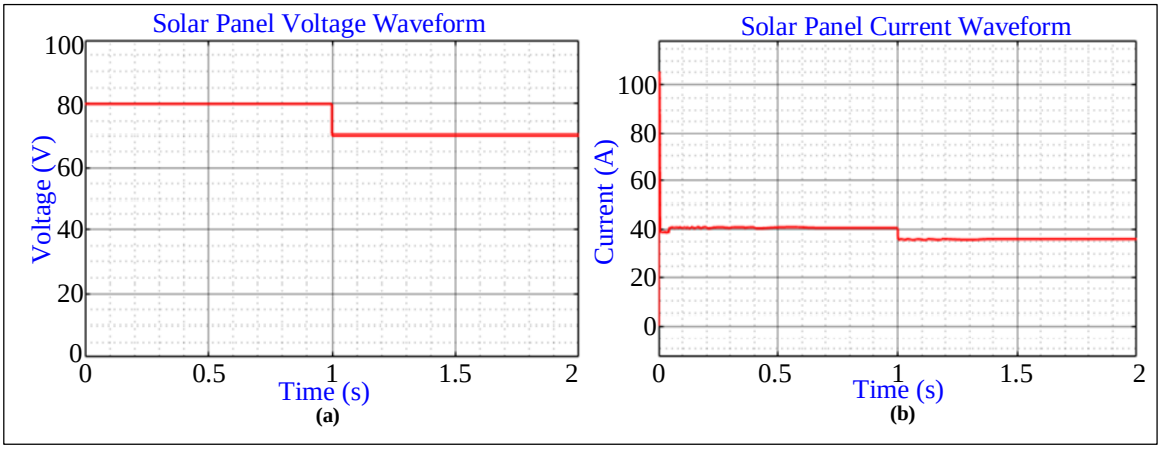

Fig. 18 Waveform of voltage and current in solar panel

Figure 18 shows the voltage waveform stabilizing at 70V in one second, as well as the current waveform stabilizing at 38A in the same amount of time. This shows that the system responded quickly and effectively to reach the appropriate voltage and current levels. For the system to operate correctly and provide dependable and consistent performance, certain characteristics must be stable. The speed with which voltage and current stabilize indicates how effective and successful the control system is at preserving the intended electrical characteristics.

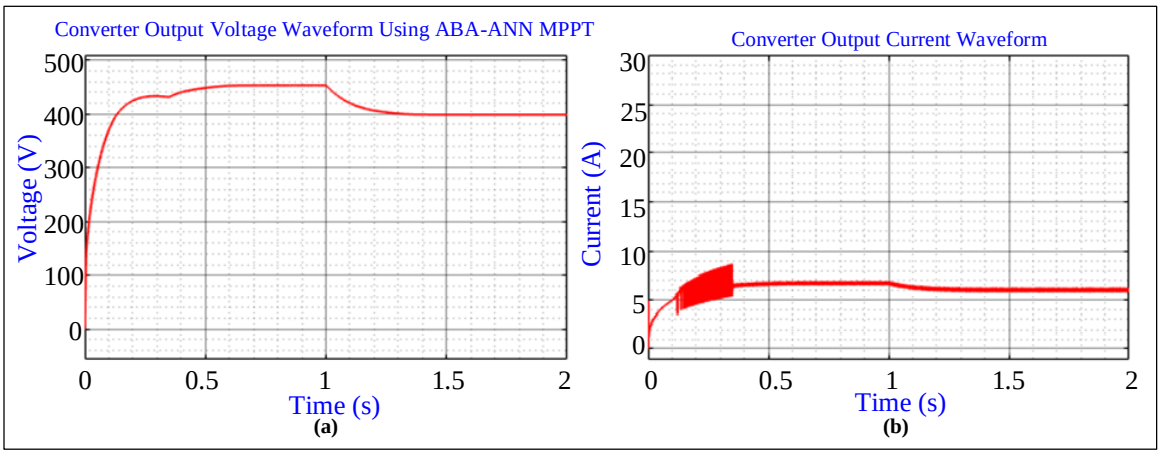

Fig. 19 (a) Using ABA-ANN MPPT waveform of converter output voltage, and (b) Converter output current waveform.

The waveform in Figure 19 shows how the voltage stabilizes at 400V in 1.5 seconds, demonstrating a quick and efficient stabilization procedure. In a similar vein, the current waveform also quickly stabilizes at 6A, taking only one second to do so. In order to keep the system functioning within the intended parameters and preserve its integrity and efficiency, these steady voltage and current levels are crucial. The system's capacity to adapt to changes and sustain steady output levels is proposed by the short stabilization times.

No Load Condition

Figure 20 presents a waveform indicating that the motor is not under any load. In this context, "no load" signifies that there is no mechanical load on the motor's shaft and no outside resistance while it operates. In this state, the behavior and performance characteristics of the motor can be seen under low stress.

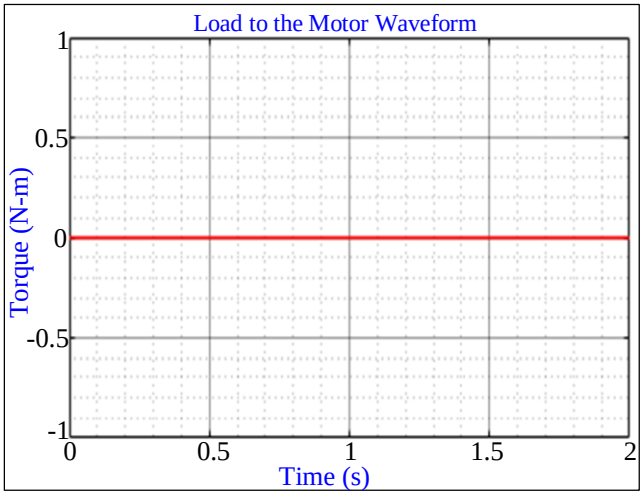

Fig. 20 Load to the motor waveform

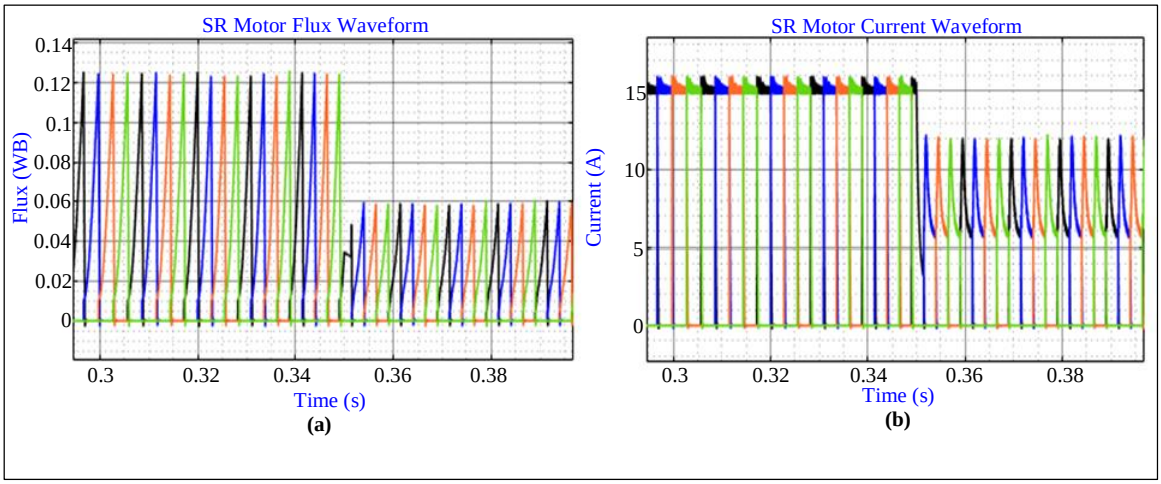

Fig. 21 (a) SR motor flux waveform, and (b) SR motor current waveform.

The following Figure 21 in waveform (a) shows us that the flux stabilizes from 0.12, then lowers and remains constantly at 0.06WB at 0.35S. Then, the SR motor current waveform shows that from 15A, it then stabilizes at 12A without any distortion at the same time where the SR motor flux remained.

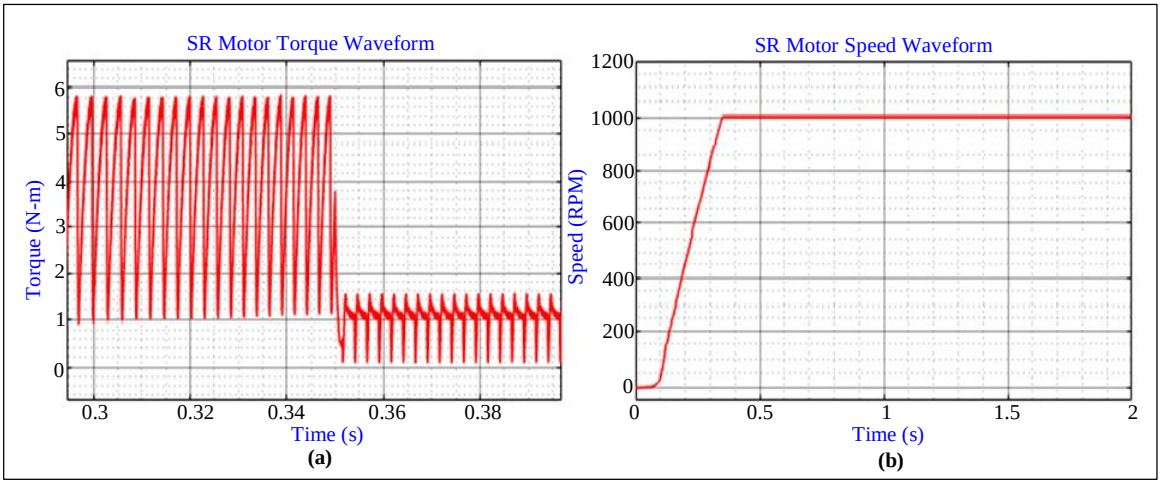

Fig. 22 (a) SR motor torque waveform, and (b) SR motor speed waveform.

The torque and speed waveforms of a Switched Resistance (SR) motor are shown in the accompanying figures as a function of time. The torque waveform is depicted in Figure 22 (a), which shows changes in torque (in N-M) over time (in seconds). According to the waveform, the torque begins at 6N-M and lowers to 1.5 N-M at 0.35S. The speed waveform in Figure 22 (b) illustrates the motor speed (in RPM) as a function of time. The speed starts at zero Revolutions Per Minute (RPM) and increases to around 1000 RPM.

0.5 N-M Load to the Motor

The waveform provided in Figure 23 illustrates the upraising of torque from 0 to 0.5N-M at 0.8S and then flows steadily.

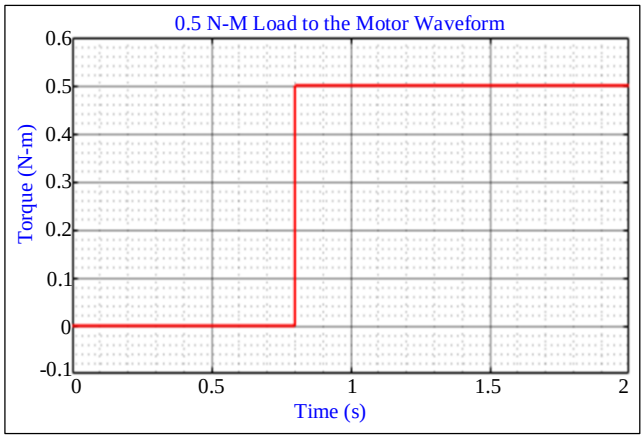

Fig. 23 0.5N-M load to the motor waveform

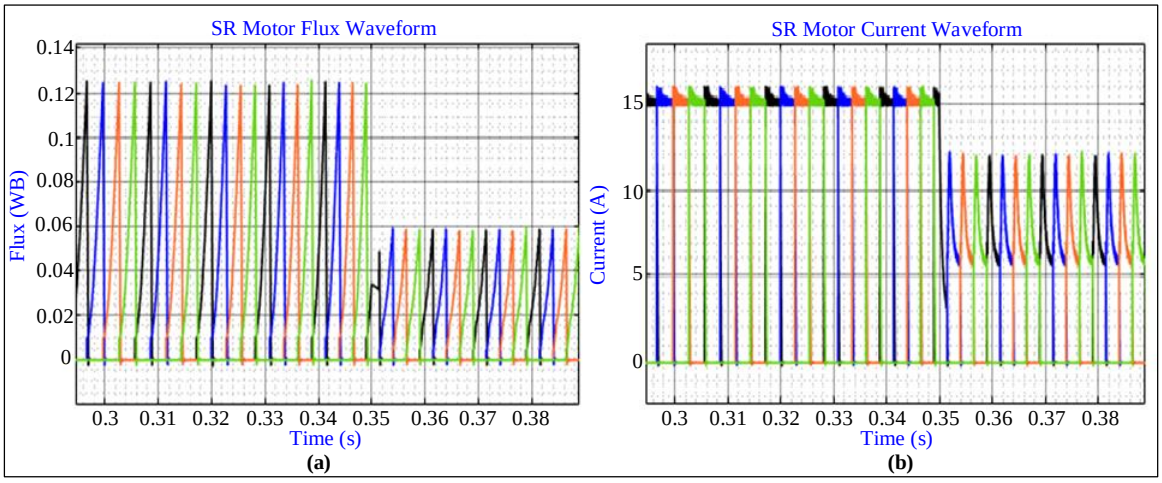

Fig. 24 (a) SR motor flux waveform, and (b) SR motor current waveform.

A Switched Reluctance (SR) motor's flux behavior is depicted in Figure 24's waveform (a). After stabilizing at 0.12, the flux drops and stays at 0.06 for the next 0.35 seconds. Meanwhile, waveform (b) shows the SR motor current, which stabilizes distortion-free at 12A, which is the same timing as the SR motor flux staying constant. The motor is in a stable operating condition when both flux and current attain steady values, guaranteeing dependable and effective motor performance. This is indicated by the synchronous stabilization.

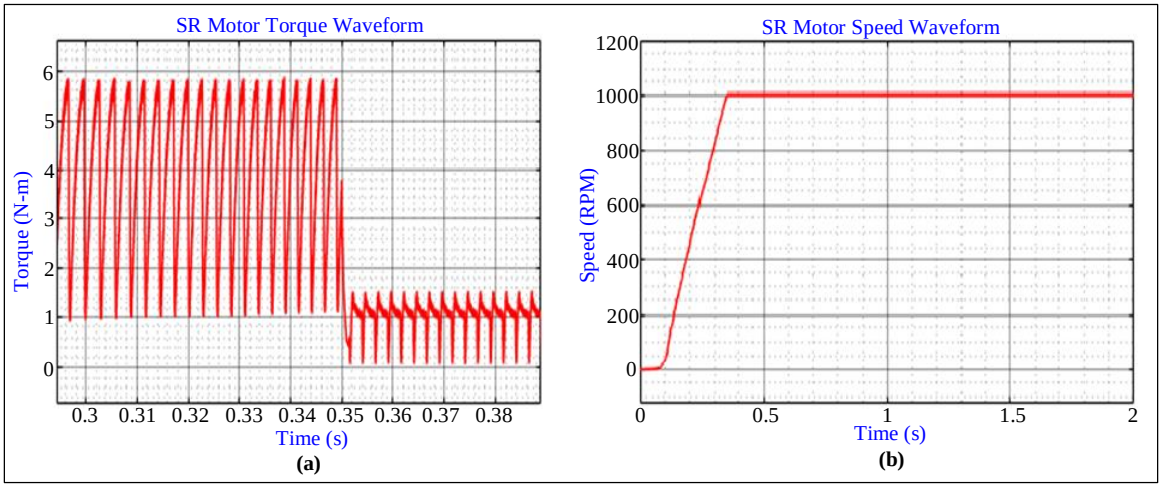

Fig. 25 (a) SR motor torque waveform, and (b) SR motor speed waveform.

The accompanying figures show the torque and speed waveforms of a Switched Reluctance (SR) motor. In Figure (a), torque increases to 1.2 N-M before decreasing, while Figure (b) illustrates speed rising and stabilizing at 1000rpm. These waveforms are essential for understanding SR motor performance.

1 N-M Load to the Motor

A waveform rising from 0 to 1 and stabilizing at 0.8 seconds is seen in Figure 26. The behavior of the waveform indicates that there was a transition from an initial condition to a steady state at 0.8 seconds, with an initial increase followed by a stabilization phase. Comprehending this waveform is essential for examining the system or process it symbolizes, offering perceptions of its stability and dynamics throughout the duration.

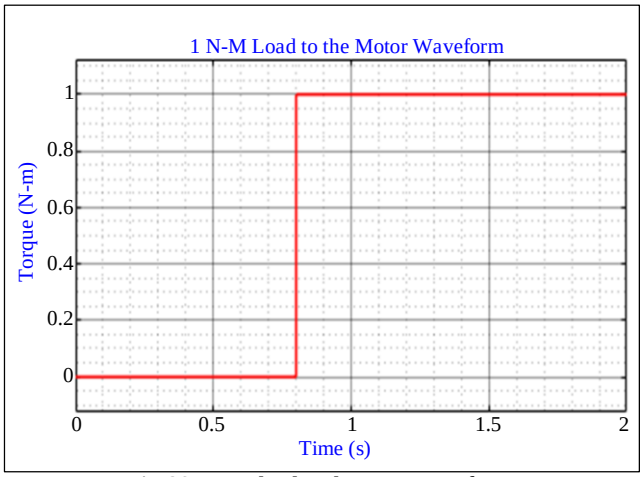

Fig. 26 1 N-M load to the motor waveform

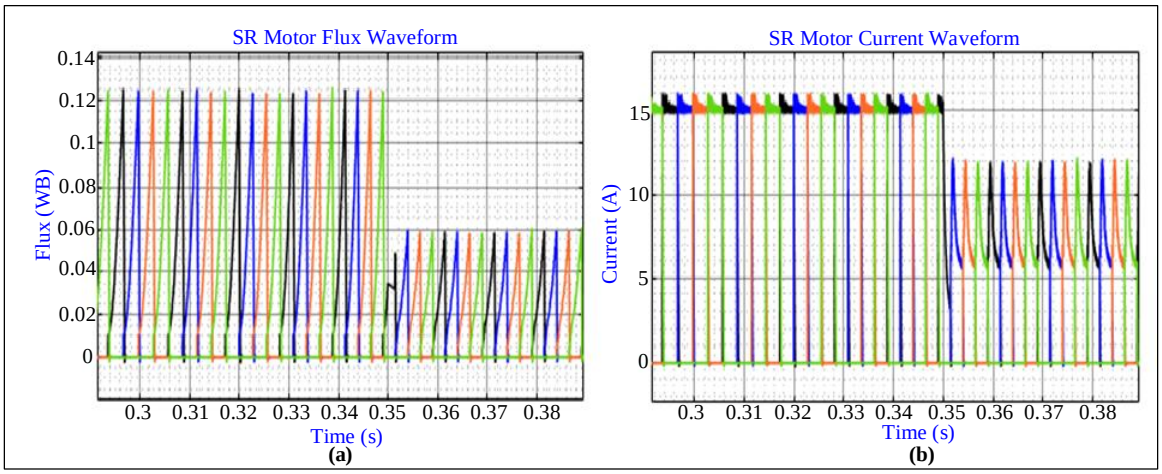

Fig. 27 (a) Flux waveform of SR motor, and (b) Current waveform of SR motor.

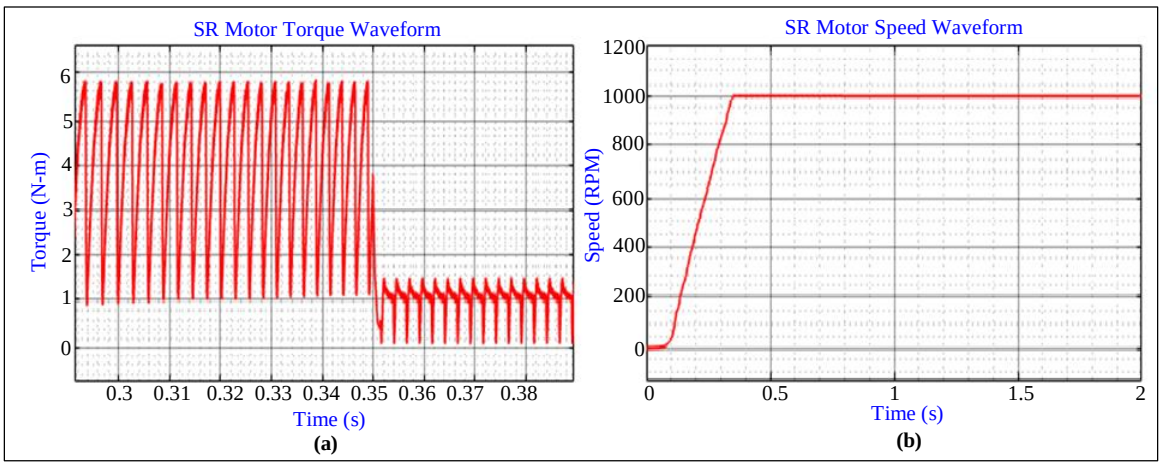

Fig. 28 (a) Torque waveform of SR motor, and (b) Speed waveform of SR motor.

Figure 27's waveform (a) shows the flux behavior of a Switched Reluctance (SR) motor. The flow decreases and remains at 0.06 for the subsequent 0.35 seconds after stabilizing at 0.12. Waveform (b) illustrates the SR motor current, which stabilizes distortion-free at 12A while the SR motor flux remains constant. When both flux and current reach steady values, the motor is said to be in a stable operating condition, which ensures dependable and efficient motor operation. The torque and speed waveforms of a Switched Reluctance (SR) motor are displayed in the accompanying

Figure 28. Figure 28 (b) shows how speed rises and stabilizes at 1000 rpm, while Figure 28 (a) shows how torque climbs to 1.2 N-M before falling. Comprehension SR motor functioning requires a comprehension of these waveforms.

Varying Condition

1.5 n-m Load to the Motor

Figure 29 shows a waveform that rises from 0 to 1.5 and stabilizes at 0.8 seconds. The waveform's behavior submits that, at 0.8 seconds, there was a change from the initial condition to a steady state, with an initial increase and a stabilization phase. Understanding this waveform is crucial to investigating the system or process it represents, providing insights into its dynamics and stability across time.

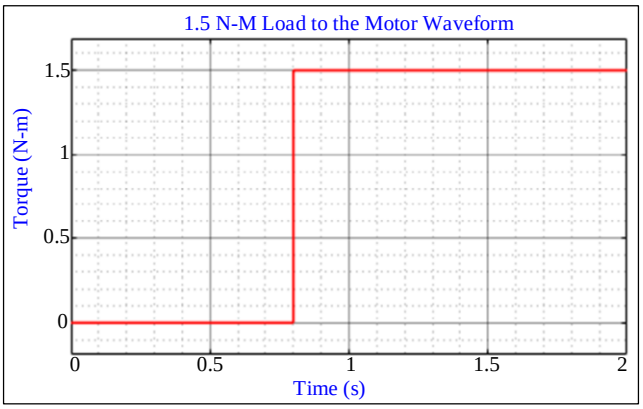

Fig. 29 Load to the motor waveform of 1.5N-M

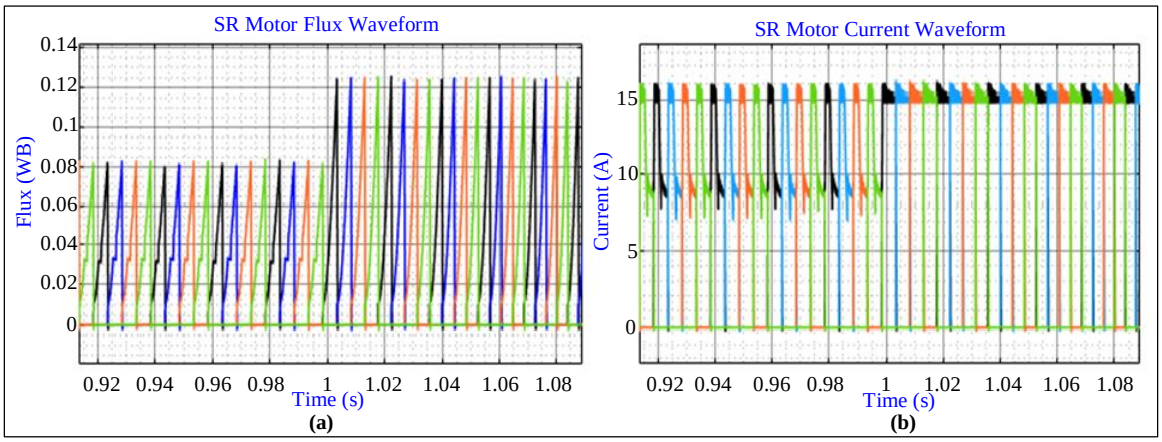

Fig. 30 (a) Waveform of flux in SR motor, and (b) Waveform of current in SR motor.

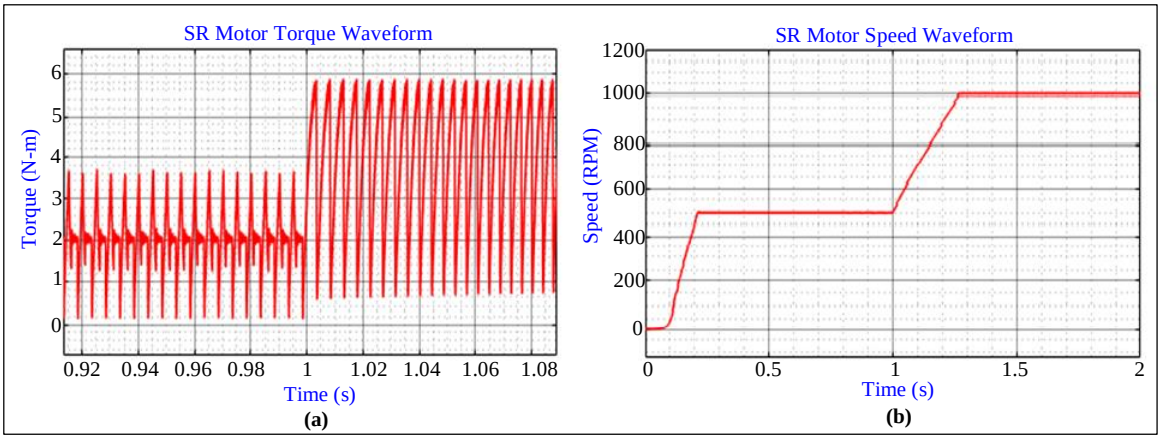

Fig. 31 (a) Waveform of torque in SR motor, and (b) Waveform of speed in SR motor.

Figure 30's waveform (a) shows how the flux increased to 0.12 WB before beginning to stabilize at one second. This waveform depicts the rise of the system's controlled flux. Waveform (b), on the other hand, displays a distortion-free, steady current waveform of 15A. This shows that the system is maintaining a steady and dependable output through a well-regulated current flow. All of these waveforms show how well the system has managed and stabilized its current and flux, which is necessary for optimal system performance.

A stabilized waveform is shown in waveform (a) of Figure 30, which grows to 6N-M at 1 second and stays at that level for the rest of the waveform. It appears from this pattern that the torque output of the system has been intentionally and carefully increased. If waveform (b) is any indication, it starts at 500 rpm and stays that way for one second before growing to 1000 rpm, which is then stable. In order to demonstrate the system's capacity to regulate and maintain speeds for optimum performance, this shows a purposeful and controlled

rise in rotating speed. Altogether, these waveforms demonstrate the system's ability to control rotational speed and torque, which is essential to its dependable and effective functioning.

4.1. Energy Storage System

A steady 100V waveform in a supercapacitor is shown in Figure 32, showing a constant voltage output free of aberrations. This waveform shows that a constant voltage level is being maintained by the supercapacitor's efficient storage and release of electrical energy.

The supercapacitor appears to be operating as intended, providing a dependable and steady voltage supply based on the lack of distortions. Such performance emphasizes the effectiveness and dependability of the supercapacitor in this situation. It is essential in many applications where a steady voltage supply is needed.

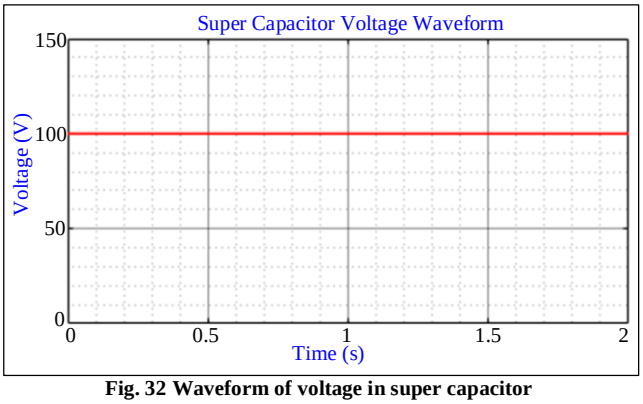

Fig. 32 Waveform of voltage in super capacitor

Table 3. Performance comparison of major electrical motors used in electric vehicle applications

Performance	DC Motors	Induction Motors	PMBL DC Motors	PMBL AC Motors	Proposed SR Motors
Power Density	L	M	H	H	H
Reliability	M	H	H	H	V.H
Efficiency	L	M	H	M	V.H
Cost	M	L	H	H	M
Size	M	M	S	S	La
Controllability	H	H	H	H	V.H
Speed Range	M	M	L	L	V.H
Maximum Torque	M	M	H	H	V.H
Torque Ripple	L	L	M	L	L

Where: L = Low, M= Medium, H = High, V.H = Very high, S = Small, and La = Large

Table 3 presents a comparison of several motor types according to multiple performance parameters. Although they are more expensive, Permanent Magnet Brushless DC (PMBL DC) and permanent magnet brushless AC (PMBL AC) motors provide excellent power density, dependability, and efficiency. Induction motors have a medium power density, medium cost, and moderate efficiency and dependability. Proposed Switched Reluctance (SR) motors, on the other hand, are more expensive and less efficient despite having a large speed range, great torque, and excellent controllability. DC motors are more costly and less dependable despite having a moderate power density and efficiency. While PMBL DC motors and DC motors are medium-sized, SR motors and PMBL AC motors are comparatively modest in size. All have considerable controllability, with the exception of DC motors. All things considered, PMBL AC motors are the most dependable and efficient choice, while SR motors give the best torque, efficiency, speed range, and controllability.

Table 4. Comparative analysis of the proposed converter with several other conventional converters

SL.No	Conventional Boost Converter [21]	Conventional Buck-Boost converter [21]	Zeta converter [21]	Proposed SEPIC-LUO Converter
Switches used	1	1	1	2
Diodes used	1	1	1	1
Capacitors used	1	1	2	2
Inductors used	1	1	2	2
Total component count	4	4	6	7
Voltage Gain	$\frac{1}{(1-D)}$	$\frac{D}{(1-D)}$	$\frac{D}{(1-D)}$	$\frac{D}{(1-D)}$
Efficiency	89%	85%	87%	90%

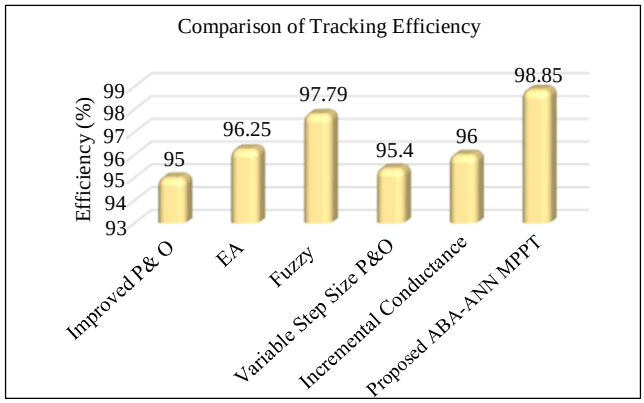

Fig. 33 Comparison of tracking efficiency

From Table 4, the variations in voltage conversion application performance and design complexity will be found by comparing different types of converters. Using four switches and one diode, the conventional boost converter and conventional buck-boost converter provide voltage gains of 1-D and 85-89% efficiency, respectively. The Zeta Converter reaches 87% efficiency with 6 switches and 1 diode. By comparison, the proposed SEPIC-LUO converter, which consists of two diodes and seven switches, runs at 90% efficiency and generates a 1-D voltage gain. These converters, which vary in component count, switch and diode usage, and efficiency levels, show the trade-offs between complexity and performance.

The tracking effectiveness of various MPPT algorithms is displayed in the comparison. The range efficiency numbers are 93% to 99.85%. The proposed African Buffalo Algorithm-Artificial Neural Network (ABA-ANN) MPPT, incremental conductance, Evolutionary Algorithms (EA), improved P&O, and fuzzy logic-based techniques are among the approaches. Every algorithm has an efficiency rating; the proposed technique has the highest efficiency of 98.85%.

5. Conclusion

This research work proposes an integrated SEPIC-Luo DC-DC converter, or High Gain Improved Single-Ended Primary Inductor Converter with Luo architecture, to optimize the output of PV systems for use in PV arrays. By continuously adjusting to environmental changes, an ANN controller optimized with the ABA maximizes the power output of photovoltaic systems. Through the use of a bi-directional converter, excess energy can be quickly stored and released as needed in a supercapacitor.

A three-phase Synchronous Reluctance Motor (SyRM) driven by a (n+1) diode and (n+1) semiconductor converter powers the EV's propulsion system. A PI controller based on a hysteresis controller regulates the motor's speed precisely. The proposed converter exhibits an efficiency of 90%, whereas the African Buffalo Algorithm-ANN based MPPT lays out a tracking efficiency of 98.85%. The entire evaluation was conducted using the simulation program MATLAB.

References

[1] Hussein Mohammed Ridha et al., "Multi-Objective Optimization and Multi-Criteria Decision-Making Methods for Optimal Design of Standalone Photovoltaic System: A Comprehensive Review," *Renewable and Sustainable Energy Reviews*, vol. 135, 2021. [CrossRef] [Google Scholar] [Publisher Link]

[2] A.T.D. Perera et al., "Quantifying the Impacts of Climate Change and Extreme Climate Events on Energy Systems," *Nature Energy*, vol. 5, pp. 150–159, 2020. [CrossRef] [Google Scholar] [Publisher Link]

[3] Joaquim Monteiro et al., "A Buck-Boost Converter with Extended Duty-Cycle Range in the Buck Voltage Region for Renewable Energy Sources," *Electronics*, vol. 12, no. 3, pp. 1-20, 2023. [CrossRef] [Google Scholar] [Publisher Link]

[4] S. Bairabathina, and S. Balamurugan, "Design and Validation of a SEPIC-Based Novel Multi-Input DC-DC Converter for Grid-Independent Hybrid Electric Vehicles," *Energies*, vol. 15, no. 15, pp. 1-27, 2022. [CrossRef] [Google Scholar] [Publisher Link]

[5] Radha Kushwaha, and Bhim Singh, "An Improved Power Factor Luo Converter Based Battery Charger for Electric Vehicle," *2020 IEEE Transportation Electrification Conference and Expo (ITEC)*, Chicago, IL, USA, pp. 723–728, 2020. [CrossRef] [Google Scholar] [Publisher Link]

[6] Jiayang Wu et al., "Frequency Folding for LLC Resonant Converters in EV Charging Applications," *IEEE Transactions on Power Electronics*, vol. 38, no. 4, pp. 5041-5054, 2023. [CrossRef] [Google Scholar] [Publisher Link]

[7] Adel Alganidi, and Amit Kumar, "PI Controller Tuning and Stability Study of the Flyback Converter with An Energy Regenerative Snubber," *2019 IEEE Canadian Conference of Electrical and Computer Engineering (CCECE)*, Edmonton, AB, Canada, pp. 1–4, 2019. [CrossRef] [Google Scholar] [Publisher Link]

[8] Linyun Xiong et al., "Output Power Quality Enhancement of PMSG with Fractional Order Sliding Mode Control," *International Journal of Electrical Power and Energy Systems*, vol. 115, 2020. [CrossRef] [Google Scholar] [Publisher Link]

[9] Xiang Zhou et al., "A High-Efficiency High-Power-Density On-Board Low-Voltage DC-DC Converter for Electric Vehicles Application," *IEEE Transactions on Power Electronics*, vol. 36, no. 11, pp. 12781-12794, 2021. [CrossRef] [Google Scholar] [Publisher Link]

[10] Salman Habib et al., "Contemporary Trends In Power Electronics Converters for Charging Solutions of Electric Vehicles," *CSEE Journal of Power and Energy Systems*, vol. 6, no. 4, pp. 911-929, 2020. [CrossRef] [Google Scholar] [Publisher Link]

[11] Dominic Savio Abraham et al., "Electric Vehicles Charging Stations' Architectures, Criteria, Power Converters, and Control Strategies in Microgrids," *Electronics*, vol. 10, no. 16, pp. 1-45, 2021. [CrossRef] [Google Scholar] [Publisher Link]

[12] S. Saravanan, and P. Usha Rani, "A Novel High Gain Interleaved Luo Dc–Dc Converter with Cascaded Fuzzy Logic Controller for PV System Application," *Journal of Electrical Engineering and Technology*, vol. 18, no. 2, pp. 925-940, 2023. [CrossRef] [Google Scholar] [Publisher Link]

[13] Premkumar Manoharan et al., "Improved Perturb and Observation Maximum Power Point Tracking Technique for Solar Photovoltaic Power Generation Systems," *IEEE Systems Journal*, vol. 15, no. 2, pp. 3024-3035, 2020. [CrossRef] [Google Scholar] [Publisher Link]

[14] Niraja Swaminathan, N. Lakshminarasamma, and Yue Cao, "A Fixed Zone Perturb and Observe MPPT Technique for a Standalone Distributed PV System," *IEEE Journal of Emerging and Selected Topics in Power Electronics*, vol. 10, no. 1, pp. 361-374, 2021. [CrossRef] [Google Scholar] [Publisher Link]

[15] Mahmoud N. Ali et al., "An Efficient Fuzzy-Logic Based Variable-Step Incremental Conductance MPPT Method for Grid-Connected PV Systems," *IEEE Access*, vol. 9, pp. 26420–26430, 2021. [CrossRef] [Google Scholar] [Publisher Link]

[16] Tehzeeb-ul Hassan et al., "A Novel Algorithm for MPPT of an Isolated PV System Using Push Pull Converter with Fuzzy Logic Controller," *Energies*, vol. 13, no. 15, pp. 1-21, 2020. [CrossRef] [Google Scholar] [Publisher Link]

[17] Shahzad Ahmed et al., "Supertwisting Sliding Mode Algorithm Based Nonlinear MPPT Control for a Solar PV System with Artificial Neural Networks Based Reference Generation," *Energies*, vol. 13, no. 14, pp. 1-24, 2020. [CrossRef] [Google Scholar] [Publisher Link]

[18] Salman Habib et al., "Contemporary Trends in Power Electronics Converters for Charging Solutions of Electric Vehicles," *CSEE Journal of Power and Energy Systems*, vol. 6, no. 4, pp. 911–929, 2020. [CrossRef] [Google Scholar] [Publisher Link]

[19] Sergio Coelho et al., "A Unified Power Converter for Solar PV and Energy Storage in DC Microgrids," *Batteries*, vol. 8, no. 10, pp. 1-15, 2022. [CrossRef] [Google Scholar] [Publisher Link]

[20] Veerapandiyan Veerasamy et al., "A Hankel Matrix Based Reduced Order Model for Stability Analysis of Hybrid Power System Using PSO-GSA Optimized Cascade PI-PD Controller for Automatic Load Frequency Control," *IEEE Access*, vol. 8, pp. 71422–71446, 2020. [CrossRef] [Google Scholar] [Publisher Link]

[21] Molla S. Hossain Lipu et al., "Review of Electric Vehicle Converter Configurations, Control Schemes and Optimizations: Challenges and Suggestions," *Electronics*, vol. 10, no. 4, pp. 1-37, 2021. [CrossRef] [Google Scholar] [Publisher Link]

[22] Pandav Kiran Maroti et al., "The State-of-the-Art of Power Electronics Converters Configurations in Electric Vehicle Technologies," *Power Electronic Devices and Components*, vol. 1, 2022. [CrossRef] [Google Scholar] [Publisher Link]

[23] Efrain Mendez et al., "Improved MPPT Algorithm for Photovoltaic Systems Based on the Earthquake Optimization Algorithm," *Energies*, vol. 13, no. 12, pp. 1-24, 2020. [CrossRef] [Google Scholar] [Publisher Link]

[24] Doudou N. Luta, and Atanda K. Raji, "Fuzzy Rule-Based and Particle Swarm Optimisation MPPT Techniques for a Fuel Cell Stack," *Energies*, vol. 12, no. 5, pp. 1-15, 2019. [CrossRef] [Google Scholar] [Publisher Link]

[25] Ahmed I.M. Ali, Mahmoud A. Sayed, and Essam E.M. Mohamed, "Modified Efficient Perturb and Observe Maximum Power Point Tracking Technique for Grid-Tied PV system," *International Journal of Electrical Power and Energy Systems*, vol. 99, pp. 192–202, 2018. [CrossRef] [Google Scholar] [Publisher Link]

[26] Nur Fairuz Mohamed Yusof, Dahaman Ishak, and Mohamed Salem, "An Improved Control Strategy for Single-Phase Single-Stage Grid-Tied PV System Based on Incremental Conductance MPPT, Modified PQ Theory, and Hysteresis Current Control," *Engineering Proceedings*, vol. 12, no. 1, pp. 1-4, 2022. [CrossRef] [Google Scholar] [Publisher Link]